



Wear Mechanisms of Cold-Sprayed Stellite-6 During Reciprocated Dry Sliding Under Different Sliding Speeds

P. Magarò¹ · F. Furgiuele¹ · C. Maletta¹ · M. Tului² · R. J. K. Wood³

Submitted: 31 January 2023 / in revised form: 17 July 2023 / Accepted: 31 July 2023 / Published online: 16 August 2023
© The Author(s) 2023

Abstract Cobalt–chromium alloys are often employed in those environments that require reliable wear and friction properties. Cold Gas Dynamic Spray offers the opportunity to obtain good quality deposits of Stellite-6, that can be successfully used in harsh environments, where good surface performance, in terms of wear resistance, is required. It is also well-known that Stellite-6 is subjected to several physical changes at the interface during dry sliding, that are often related to the loading conditions. As a consequence, wear behavior of this alloy can undergo some variations that linear models are not able to capture, since micro-structural modifications occur during operation. To better understand the wear mechanisms of cold-sprayed Stellite-6 coatings together with the occurring physical phenomena, a systematic experimental study was performed, in fact, to date, no such in-depth tribological studies have been performed. Tests were conducted under combinations of two sliding speeds (0.1 and 0.5 m/s) and four contact pressure in the range of 2–5 MPa. In low-speed tests, abrasive wear is evident, where detachment and pull-out phenomena mainly affect the worn surface of coatings. On the other hand, subsurface cracking was observed in high-speed tests, as well as evidence of plastic deformation on the

wear surface. These results suggest that observed wear mechanisms are more likely a consequence of adhesive wear. Unique to this study, the cross-sectional nano-indentation tests showed how the stiffness of the coating, near to wear interface, increases significantly in the case of the lowest value of sliding speed (i.e., $v = 0.1$ m/s), whereas tends to decrease at high speeds, i.e., $v = 0.5$ m/s, as a consequence of the formation of subsurface cracks into the coating.

Keywords cold gas dynamic spray · dry sliding · indentation · platelet · pull-out · stellite

Introduction

Cobalt-based alloys are used in several applications, such as oil industry (critical components of drilling), electrical industry (energy-generating turbines), automotive industry (coatings on exhaust parts), and others (Ref 1, 2) due to their excellent wear, corrosion, and oxidation resistance (Ref 3). In fact, in surface engineering, Stellite alloys are widely used in order to protect various components against wear, corrosion, and oxidation. These properties are given by the high chromium content and thanks to the presence of carbides and borides coupled with lattice stress-induced transitions occurring in the contact region under high-load sliding conditions. This latter phenomenon provides remarkably high hardness and good wear properties thanks to the formation of hexagonal close-packed structures, which are caused by shear stress during the contact in place of the parent face-centered one (Ref 4, 5). In order to obtain good Stellite coatings, different deposition technologies can be used, e.g., plasma transferred arc (PTA) (Ref 6) or tungsten inert gas (TIG) welding (Ref 7), thermal spraying

✉ P. Magarò
pietro.magarò@unical.it

¹ Department of Mechanical, Energy and Management Engineering, University of Calabria, 87036 Arcavacata di Rende, Italy

² CSM SpA, Lamezia Terme Branch Office, Zona Industriale San Pietro Lametino, 88046 Lamezia Terme, Italy

³ National Centre for Advanced Tribology Southampton (nCATS), Faculty of Engineering and the Environment, University of Southampton, Southampton SO17 1BJ, UK

(Ref 8-15) or laser cladding (Ref 16-23), that implies some differences in the coating microstructures and consequently in the coating properties. Within the class of thermal spraying technologies, Cold Gas Dynamic Spray (CGDS) represents an interesting option to deposit good Stellite coatings. This technology consists in a process in which solid powders are accelerated in a de Laval nozzle toward a substrate by a supersonic jet of high-pressure gas. Moreover, the temperature reached by the sprayed particles during the process is below the melting temperature of the material. Due to the adiabatic shear instability, that occurs thanks to the high strain rate, the particles can undergo large plastic deformation, so the material flow provides the required heat for bonding. This phenomenon represents the main driving force for the adhesion of the coating to the substrate (Ref 24-27). In fact, CGDS technique has been successfully applied in the last years for the deposition of ductile metals such as copper and aluminum-based alloys, due to their remarkable ductility (Ref 28-31)

Particle bonding, in turn, occurs if particle velocity reaches a threshold value called critical velocity, which is influenced by the mechanical and physical properties of the sprayed material i.e., size, distribution, and morphology. In this regard, Schmidt et al. developed an equation to find the critical velocity, as reported in ref. (Ref 25), as a function of temperature-dependent flow stress, density, heat capacity, melting temperature of the sprayed material and particle temperature upon impact.

This technique has the advantage, in spite of conventional ones, of producing highly compact deposits and oxide-free structures preventing tensile residual stresses and chemical contamination. Furthermore, there is still a limited understanding on how the loading conditions affect the physical response of the alloy and in turn how they influence the wear mechanisms.

While the general wear response of such alloys has been investigated experimentally, with a focus on common thermal sprayed Stellite coatings, there have not been to date many studies on the understanding of the wear mechanisms that occur, as a result of the loading conditions, for cold spray deposits such as carbide pull-out and fracture (Ref 32, delamination (Ref 33) and fatigue of a wear-reducing oxide layer (Ref 34. The use of a mechanistic model of wear, that can capture the physical response of the system as a consequence of the loading conditions and environment, would be useful to understand the coating behavior in situ. Typically, the Archard wear equation (Ref 35) is used to estimate the material performance:

$$V = K \frac{N \times s}{H} \quad (\text{Eq 1})$$

where V is the total volume of wear debris produced, K is a dimensionless constant that is obtained from

experimental results, H is the hardness of the surface, N is the normal load, and s is the total sliding distance. This model suggests that, for a given system, the wear behavior is linear with sliding distance and normal load, like other literature wear models usually employed to characterize the wear behavior of the material system (Ref 35, 36). The latter do not capture the physic phenomena involved during the sliding. Changes in the environment and loading conditions have to be considered for the development of a model that can take into account these aspects. However, to date, no in-depth studies on the effects of load and sliding speed, at room temperature, have been performed in the case of cold-sprayed Stellite coatings. Therefore, this paper aims to understand how loading conditions can influence the wear mechanisms of cold-sprayed Stellite deposits and to identify the significant physical phenomena occurring at the wear surface. New insight can allow the development of proper models, able to predict the wear coefficient of these kinds of coatings. Several analysis techniques have been used to determine the wear mechanisms in this study. Wear surfaces and cross sections of the samples, tested under different sliding conditions, were examined under light and scanning electron microscope. In addition, post-wear nano-indentation measurements into the subsurface of the coatings have been performed to clarify how the wear mechanisms can modify the mechanical properties of the coating. Frictional data were also collected and analyzed. The experimental procedure is described in “Materials and Methods” Section. Results are presented and discussed in “Results and Discussion” Section. Finally, conclusions are provided in “Conclusions” Section.

Materials and Methods

Coating Process

A commercial Stellite-6 powder (Diamalloy 4060NS, Oerlikon Metco, Switzerland) obtained by gas atomization, with particle size $-45 + 15 \mu\text{m}$, was employed as a feedstock. Table 1 reports the chemical composition, provided by the supplier, for the powder.

Stainless steel (AISI 304) plates of dimension $20 \times 60 \times 3 \text{ mm}$ were coated using a high-pressure CGDS equipment (Impact Spray System 5/11, Impact Innovation, Germany) equipped with a pre-chamber of

Table 1 Chemical composition of Diamalloy 4060NS, wt.%

Co	Cr	W	Fe	C	Si	Other
Bal.	28.5	4.5	≤ 3.0	1.08	1.6	< 0.5

135 mm in length. Nitrogen was used as process gas. Spraying conditions were optimized from previous studies (Ref 37, 38) and were as follows: gas temperature and pressure equal to 970 °C and 4 MPa, respectively, and stand-off distance equal to 20 mm. Traverse gun speed was set equal to 300 mm/s, while coatings were obtained from three spraying layers.

Coating Characterization

CGDS deposits were examined by an optical microscope (DM4000 M, Leica, Germany) equipped with a high-resolution camera (MC190 HD, Leica, Germany). For this purpose, samples were cut, mounted using epoxy resin, grinded using wet SiC grinding papers, and polished using diamond solution and silica, both with polishing cloths.

Coating microstructure was revealed by etching with a mixture of acids (15 mL HNO₃, 15 mL CH₃COOH, 60 mL HCl and 20 mL of H₂O) and reported in the following section.

Porosity content was also estimated using the image analysis software Image J. However, according to the standard ASTM E2109.

Tribological Characterization

The experimental tests were carried out on a reciprocating sliding test rig, i.e., TE77 (Phoenix Tribology, Berkshire, UK) in dry room condition, i.e., temperature around 25 °C and relative humidity around 40%. A schematic depiction of the test equipment is in Fig. 1.

Frictional data, i.e., the evolution of coefficient of friction, were recorded using a transducer connected to the TE77 rig. The wear tests were performed to evaluate the influence of the sliding speed and applied load on the wear mechanisms. The experimental campaign has been developed in order to deeply investigate the wear performance of Stellite-6 coating in the range between 2 and 5 MPa. Sliding distance was kept constant for all experiments and set equal to 500 m with a stroke length equal to 26.4 mm. The full test matrix is reported in Table 2. Finally, three experiments have been performed for each load condition.

The sliding geometry chosen was an “area-on-flat” with a cylindrical pin of 7.94 mm diameter realized in chromium *AISI 52100* steel. This latter material was hardened to 60-67 Rockwell Scale equivalent to 700-900 HV (Vickers Scale). Pins were slid against plates of dimension 20 × 60 × 3 mm. Each sample was polished using diamond solution obtaining a surface finish of 0.2 μm ± 0.05 average roughness (R_a), in order to replicate a contact system that reflects a typical industrial application. Surface roughness was measured using a contact profilometer (Talysurf, Taylor-Hobson, UK). Post-wear characterization consisted of weight measurements for both plate and pin and, from this data, the wear coefficient W [mm³/Nm] was calculated using the following equation:

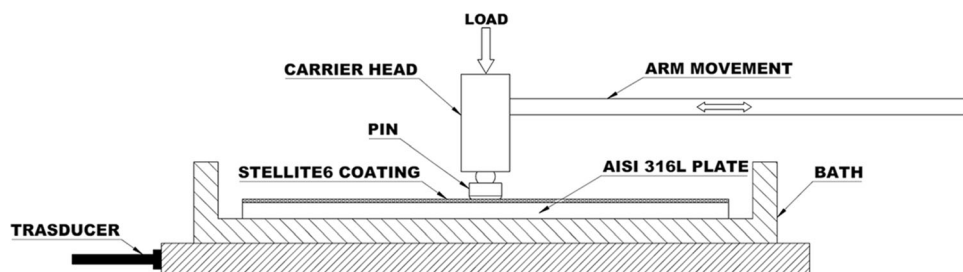
$$W = \frac{V}{N \times s} \quad (\text{Eq 2})$$

where V is the volume loss [mm³], N [N] is the load, and s [m] is the sliding distance. In order to determine the volume loss, the mass loss was divided by the density of the Stellite-6 powder and steel, respectively, for plate and pin, i.e., 8.44 g/cm³ and 7.8 g/cm³. After each experiment, plates and pins were cleaned in an isopropanol ultrasonic bath to exclude the presence of debris in the weight measurement. These latter, in fact, should be considered as “cut-out” material that would tend to compromise the weight measurements for the calculation of mass and volume loss.

Table 2 Range of parameters used in different combinations for wear tests

Load, N	Pressure, MPa	Velocity, m/s
100	2	0.1
150	3	
200	4	
250	5	
100	2	0.5
150	3	
200	4	
250	5	

Fig. 1 Schematic depiction of the experimental equipment



The post-wear surface of the Stellite coatings was characterized using a Scanning Electron Microscope (JEOL JSM-6500).

The evolution of microscopic material properties after wear tests was evaluated using the nano-indentation method, using a nano-indenter (NHT, CSM Instruments, Switzerland) equipped with a Berkovich diamond tip.

Results and Discussion

Microstructure of the Coating

Figure 2 shows the cross section of Stellite-6 coatings. High compactness can be observed (see Fig. 2a) and, as explained in the previous section, the porosity content has been estimated through image analysis. In particular, it was found that the porosity content is equal to 1.9%.

In Fig. 2(b) can be observed how the particle boundaries maintain their round shape and this result can be related to the resistance to deformation of the Stellite-6 powder.

In addition, Fig. 2(b) shows how the deposition mechanisms involve mechanical deformation of both sprayed particles and substrate at the impact interface. In fact, it is possible to observe that, despite the substrate has been just grounded before deposition, the substrate-coating interface shows the rounded profile of the impacted particles as a consequence of the higher Stellite-6 hardness compared to the steel substrate. Moreover, Fig. 2(c), (d) and (e) reports the detailed characteristics of the dendrite deformation within the particles, typical of the Co-Cr systems.

Friction and Wear Mechanisms

Figure 3 reports the trends of the dynamic coefficient of friction obtained from reciprocating sliding wear

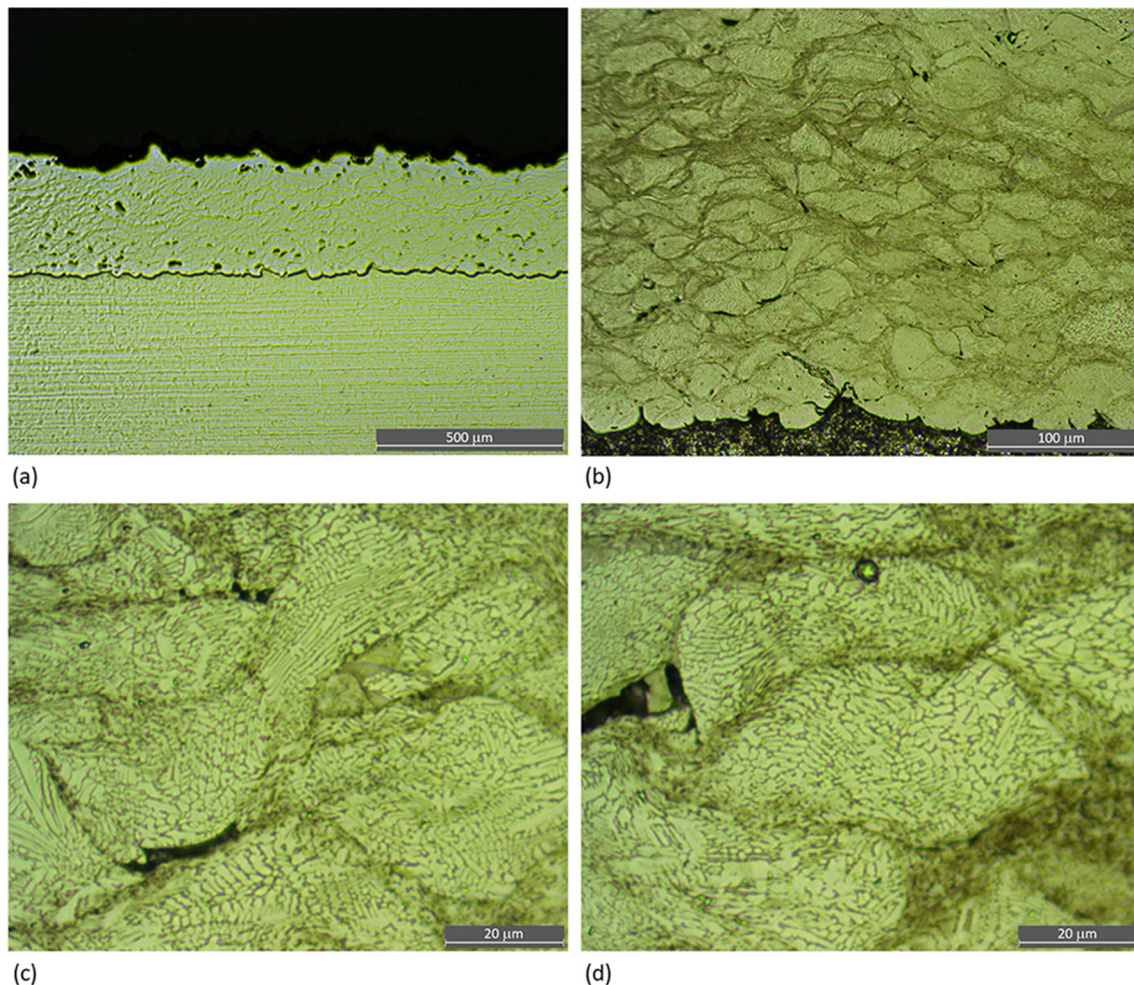


Fig. 2 Optical cross section of the coating at different magnifications: (a) & (b) low magnification level, (c) & (d) detailed features of the dendrite deformation in the particles

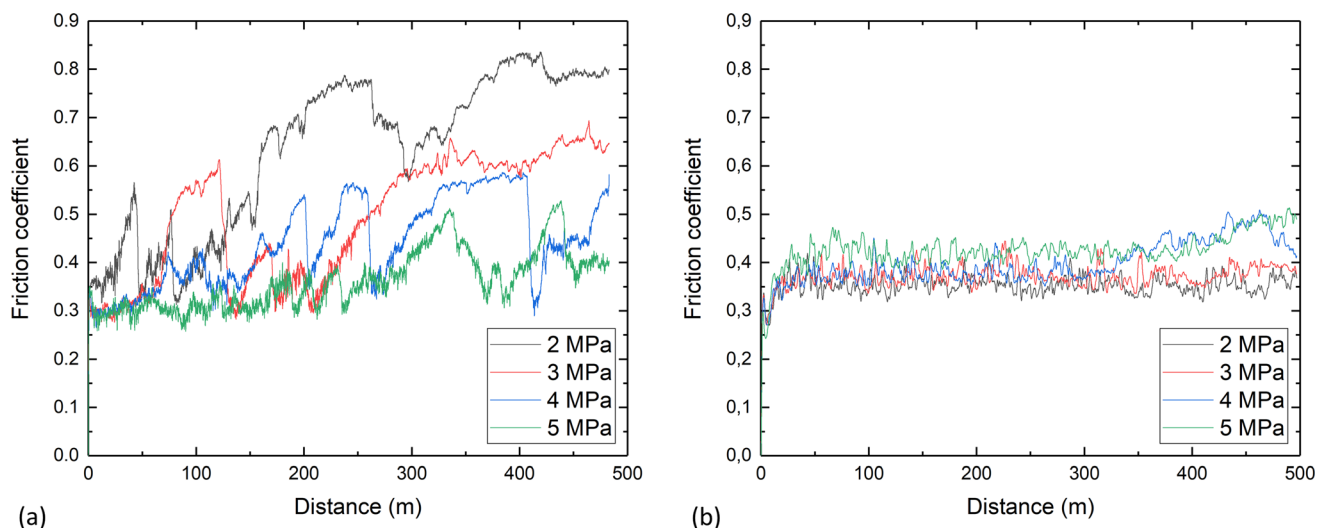


Fig. 3 Friction coefficient of Stellite-6 samples submitted to reciprocating sliding wear under different values of contact pressure and at different sliding speeds: (a) $v = 0.1$ m/s and (b) $v = 0.5$ m/s

experiments as a function of the sliding distance, for each value of the contact pressure and sliding speeds (see Table 2).

Different trends are observed comparing the results at low and high sliding speeds. Nonuniform peak and valley trends were captured in the case of low speed, characterized by rapid increases followed by sudden drops, and these effects are more evident at low contact pressures (2 and 3 MPa). On the contrary, nearly constant trends were recorded at the higher sliding speed (0.5 m/s).

Figure 4 summarizes the average values of the frictional data, obtained through the entire sliding distance, for the different values of the contact pressure and speed reported in Table 2. Corresponding scatter bars are also shown. The coefficient of friction tends to decrease with increasing the contact pressure for low sliding speed ($v = 0.1$ m/s), varying in the range of 0.4–0.65. On the contrary, a slight increase with the contact pressure is observed at higher speed ($v = 0.5$ m/s), which is in the range of 0.35 to 0.45. Very large scatters can be observed at low speed, especially for the experiments carried out setting the contact pressure equal to 2 and 3 MPa, due to the remarkable nonuniform trend shown in Fig. 3(a). These behaviors are attributed to distinct wear mechanisms. To this aim, systematic analyses of the wear track were carried out by SEM micrographic investigations with the purpose to capture possible local effects like pull-out phenomena, abrasion, adhesion mechanisms, and crack propagation in the wear surface.

Figure 5 shows representative cross sections, perpendicular to the sliding direction, of worn samples. Micrograph images of the samples tested at $v = 0.1$ m/s do not show subsurface cracks along with the thickness of the

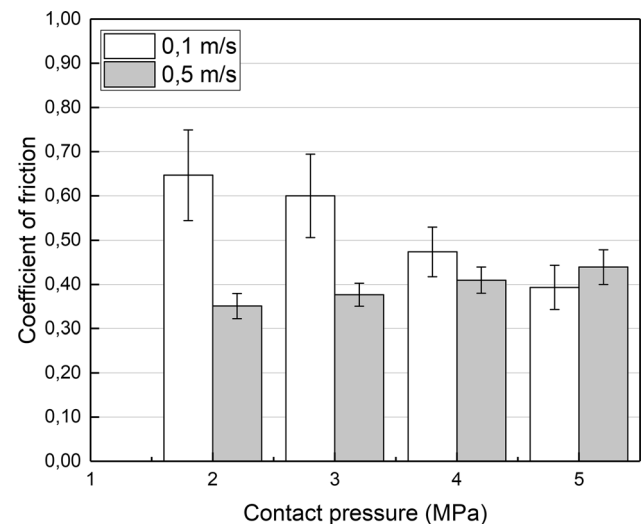


Fig. 4 Evolution of dynamic coefficient of friction as a function of contact pressure for both values of sliding speed tested

coating (see Fig. 5a, b and c). On the contrary, subsurface cracks are formed during tests carried out at high speed, i.e., $v = 0.5$ m/s (see Fig. 5d, e, and f), suggesting that wear mechanisms are mainly affected by the sliding speed. Nevertheless, the involved wear mechanisms will be better addressed in the following sections, where SEM micrographs of the wear surface are reported and discussed.

Low Sliding Speed

Figure 6(a) and (b) reports the evolution of volume loss and wear coefficient as a function of the contact pressure. The volume loss experienced corresponds to a wear coefficient of the order of 2×10^{-5} – 5×10^{-5} mm³/Nm and

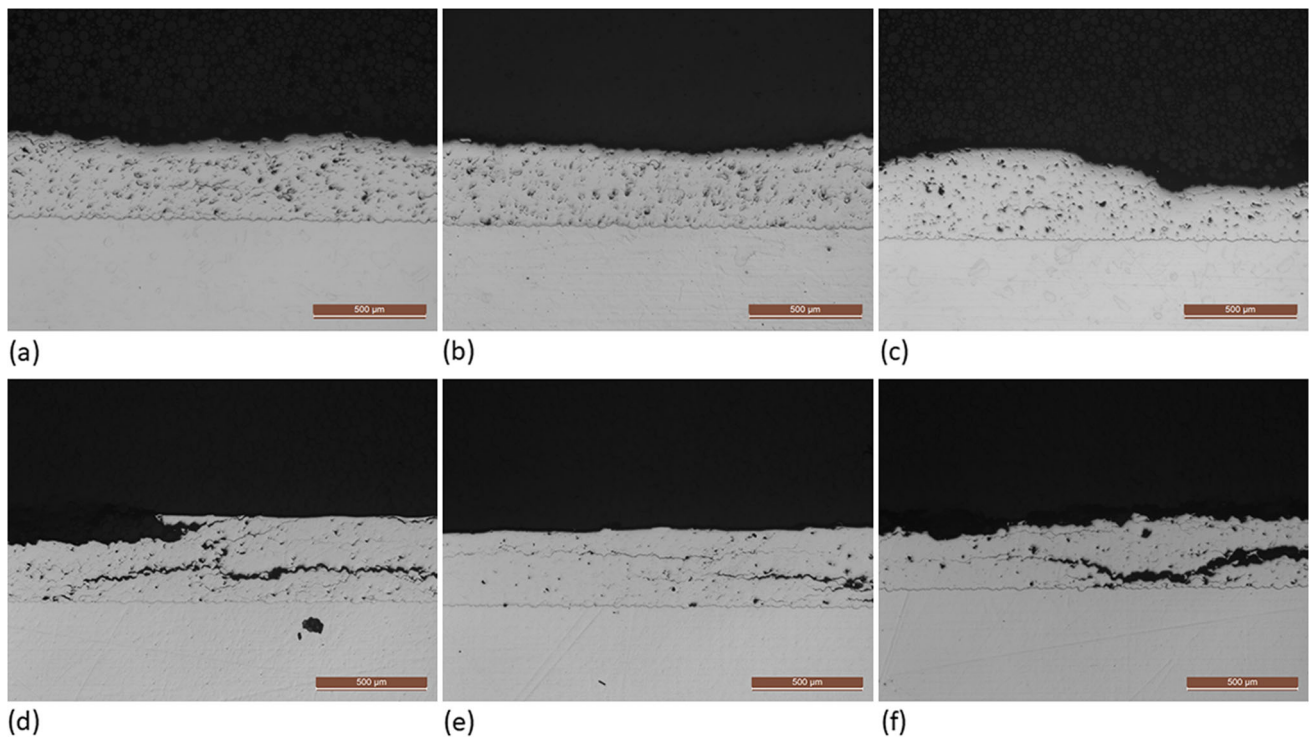


Fig. 5 Representative light micrographs of the samples cross sections for different levels of contact pressure and sliding speed: (a) 2 MPa-0.1 m/s, (b) 3 MPa-0.1 m/s, (c) 4 MPa-0.1 m/s, (d) 2 MPa-0.5 m/s, (e) 3 MPa-0.5 m/s, (f) 4 MPa-0.5 m/s

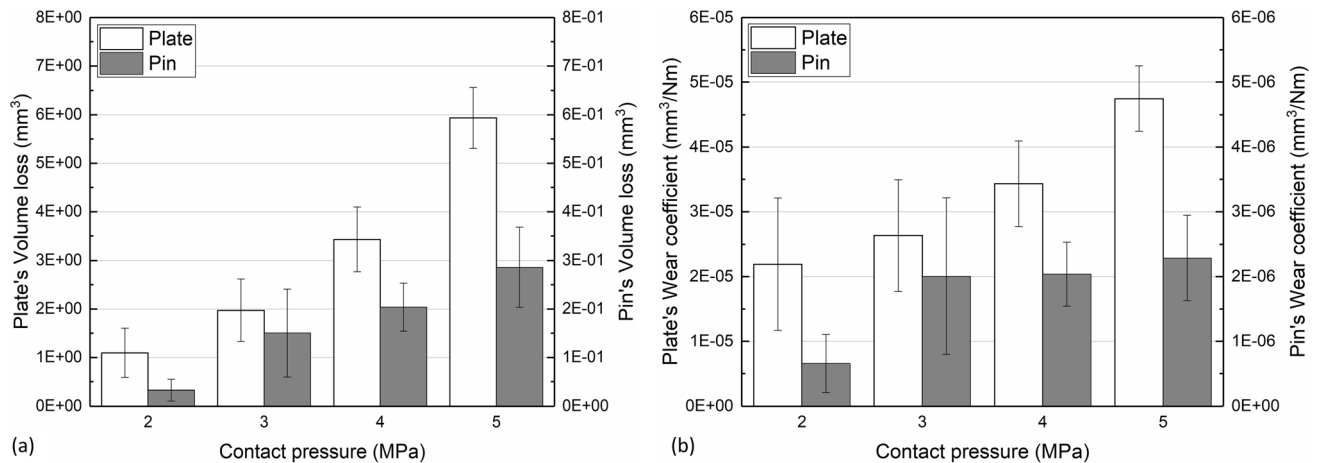


Fig. 6 Volume loss and wear coefficient vs. contact pressure plots for 0.1 m/s

6.5×10^{-7} - 2.5×10^{-6} mm³/Nm for the plate and pin, respectively. It is interesting to note how the obtained results show a nonlinear trend in the volume loss, and so in a non-constant trend of the wear coefficient. Therefore this material system is not in agreement with Archard's model in its wear behavior and thus not Archard-like according to Eq (1). Both values tend to increase increasing the contact pressure as a consequence of the higher density of pull-out phenomena, and as confirmed by the microscopic observation that will be further discussed below.

The highest value of the contact pressure, in fact, leads to the greatest value of both volume loss and wear coefficient as a direct consequence of the increased pull-out phenomena and grain wear. A confirmation of the occurrence of pull-out phenomena during the sliding at low speed can be found in the evolution of the dynamic friction coefficient as a function of the sliding distance for all values of the contact pressure as shown in Fig. 3(a). The sudden variations of friction coefficient, observed during the low-speed tests, correspond with delamination ignition

and consequent detachment of splats that tend to form a tribo-film consisting reasonably of oxidized wear debris. This phenomenon is observable on the wear track as displaced material, and acts as solid lubricant. Therefore, the dynamic friction coefficient tends to decrease by increasing the contact pressure as shown in Fig. 4. Due to the significant increase in both volume loss and wear coefficient with the contact pressure (see Fig. 6), it is reasonable to assume that the amount of tribo-film on the wear track increase with the contact pressure.

Compared to the experiments carried out by Cross et al (Ref 39), where the material was processed using a HIPing cycle of 100 MPa at 1200 °C for 4 h, the average value of the measured wear coefficients is two orders of magnitude greater. This result can be considered a direct consequence of the weakness of the inter-particle boundaries that represents a technical issue to overcome when cold-sprayed Stellite coating was used in sliding conditions.

In fact, pull-out of splats contributes to increasing the mass loss at the end of the test, whereas debris tends to increase the severity of the abrasion mechanism.

Figure 7 shows post-wear SEM micrographs of the worn surface of samples tested at increasing values of the contact pressure, from 2 to 5 MPa. The wear mechanism seems to be mainly abrasive throughout all experiments with evidence of pull-out phenomena. This assumption seems to be confirmed by the micrographic observations of the cross section of the samples (see Fig. 5a, b and c) that do not show subsuperficial cracks confirming the formation of pulled-out debris while running tests.

In the case of low sliding speed delamination phenomena were also observed, as the worn surface appears to be characterized by visible sharp edges as a consequence of the abrasive effects. The higher magnification SEM images revealed that delamination occurred mainly on the inter-splat boundaries (see Fig. 7b, d, f, and h), suggesting that this latter is the weak point of the coating. The sudden variations of COF (see Fig. 3a) during the tests correspond, in fact, with the delamination initiation and with the consequent pull-out phenomena occurring in the wear track. In addition, plowing can be observed on the worn surface and can be considered the main wear mechanism in those regions that are not affected by delamination and pull-out phenomena. In addition, evidence of strained and displaced material across the wear surface is seen in all tests, therefore the creation of tribofilm can be expected on the wear surface.

This observation is in agreement with the coefficient of friction results (see Fig. 3a and 4), in fact, the increase in oxidized material, as a consequence of the increasing wear debris on the worn surface, can be considered the main reason for the decreasing trend of the COF as a function of the contact pressure.

Figure 8 shows the post-wear SEM micrographs, from 2 to 5 MPa, for the pins' wear surface. Deformed material can be identified as trapped wear debris. These latter are visible on the worn surface and appear deformed, transferred, and adhered to the worn surface.

In addition, in Fig. 8(d) it is possible to observe how the material is displaced on the worn surface of the pin. This type of deformation is characteristic of the tests carried out setting the contact pressure equal to 5 MPa.

It can be summarized that in all tests carried out at low sliding speed, i.e., $v = 0.1$ m/s, wear mechanisms seem to be a consequence of the formation of solid debris on the worn surface resulting in pull-out phenomena, that are observable in all tested samples. This phenomenon appears to be typical after wear tests for CoCr alloys (Ref 3 and in particular for thermal-spray coatings where the splat boundaries usually represent the weak point of the system, leading to a type of fatigue wear named “*grain wear*” (Ref 40). This latter consists of pulled-out grains that form small flattened oxidized particles on the wear surface. This phenomenon can be considered the main reason for the reduction in the dynamic coefficient of friction as a function of the contact pressure, (see Fig. 4) since these particles act as solid lubricant.

High Sliding Speed

Figure 9 shows the evolution of volume loss and wear coefficient, as a function of the contact pressure, for the high sliding speed tests ($v = 0.5$ m/s). In this case, a linear trend can be seen for the volume loss (see Fig. 9a) and therefore an almost constant wear coefficient trend, as shown in Fig. 9(b). In addition, the dynamic friction coefficient at $p = 2$ MPa is the lowest among all the experiments, as shown in Fig. 4. This latter result can be attributed to two mechanisms: (i) the higher temperatures reached in the contact zone as a consequence of the higher value of the sliding speed; (ii) limited adhesion phenomena as a consequence of the low contact pressure that leave the place to the presence of oxidized material on the wear track that tends to form a tribo-film (Ref 4) with a reduction in the friction coefficient during the test.

In particular, the obtained results show that the wear coefficient is in the order of $\sim 2 \times 10^{-4}$ mm³/Nm and 2.75×10^{-6} – 2×10^{-5} mm³/Nm for the plate and pin, respectively, which are by an order of magnitude greater than literature data for the same testing conditions reported by Cross et al. (Ref 39) for a HIPed cobalt-chromium alloy. The presence of internal porosity, in fact, and the consequent crack initiation and propagation are responsible for the severe wear mechanisms discussed in this section.

Figure 10 reports the representative post-wear micrographs of the wear surfaces for the samples tested at

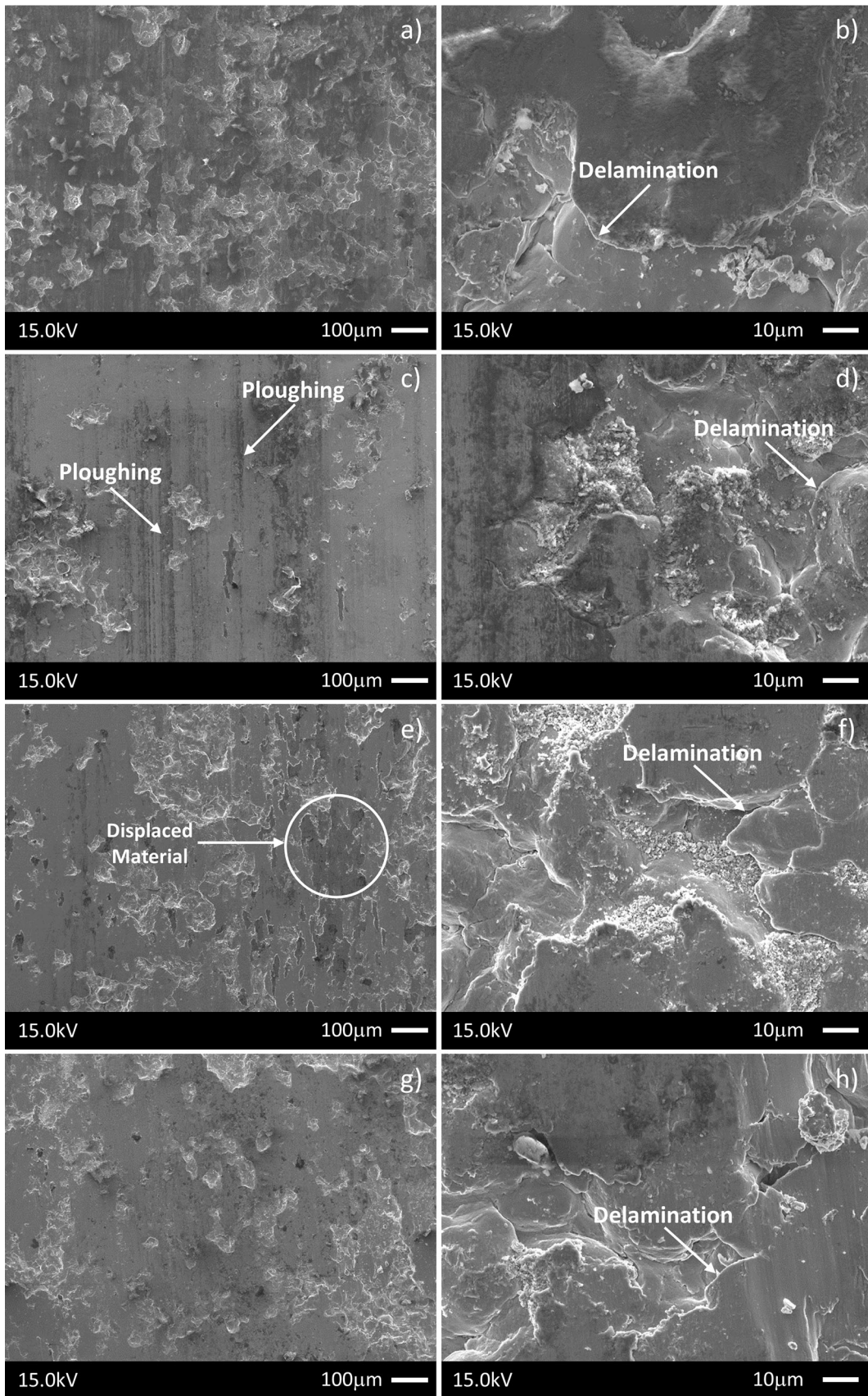


Fig. 7 Representative SEM micrograph of the wear surface on the samples tested at the sliding speed $v = 0.1$ m/s under different contact pressure: (a) and (b) $p = 2$ MPa, (c) and (d) $p = 3$ MPa, (e) and (f) $p = 4$ MPa, (g) and (h) $p = 5$ MPa

$v = 0.5$ m/s and under increasing values of the contact pressure, from 2 to 5 MPa. Adhesive wear can be seen in all tested samples. Formation of platelet can be seen on the worn surface, in particular for those samples tested under 2 MPa of the contact pressure. This latter can be

considered peeling from the surface, as seen in Fig. 10(b). Moreover, material appears adhered and pushed on the wear track, with evidence of pressed and displaced material across the surface, as can be seen in Fig. 10(d), (f), and (h). In addition, in Fig. 10 (h) it is clearly visible the presence of ridges that are due to the displacement of material.

The high-magnification images show the presence of debris on the wear surface that tend to increase increasing the contact pressure. The below layers of the coating cannot be seen either at high magnifications, as can be observed in the wear surface of the samples tested in low-

Fig. 8 Representative SEM micrograph of the wear surface on the pin at the sliding speed $v = 0.1$ m/s under different contact pressure: (a) $p = 2$ MPa, (b) $p = 3$ MPa, (c) $p = 4$ MPa, (d) $p = 5$ MPa

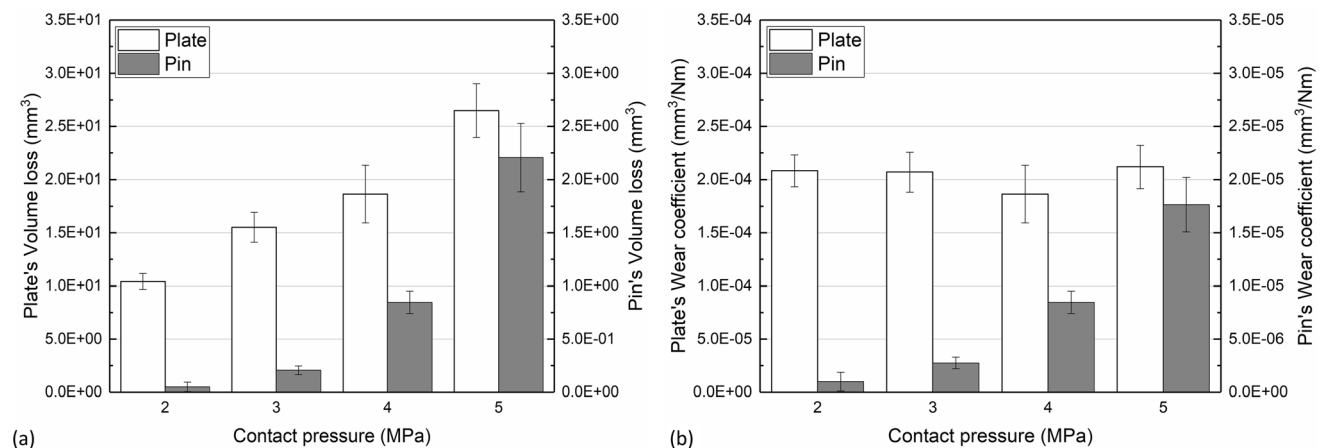
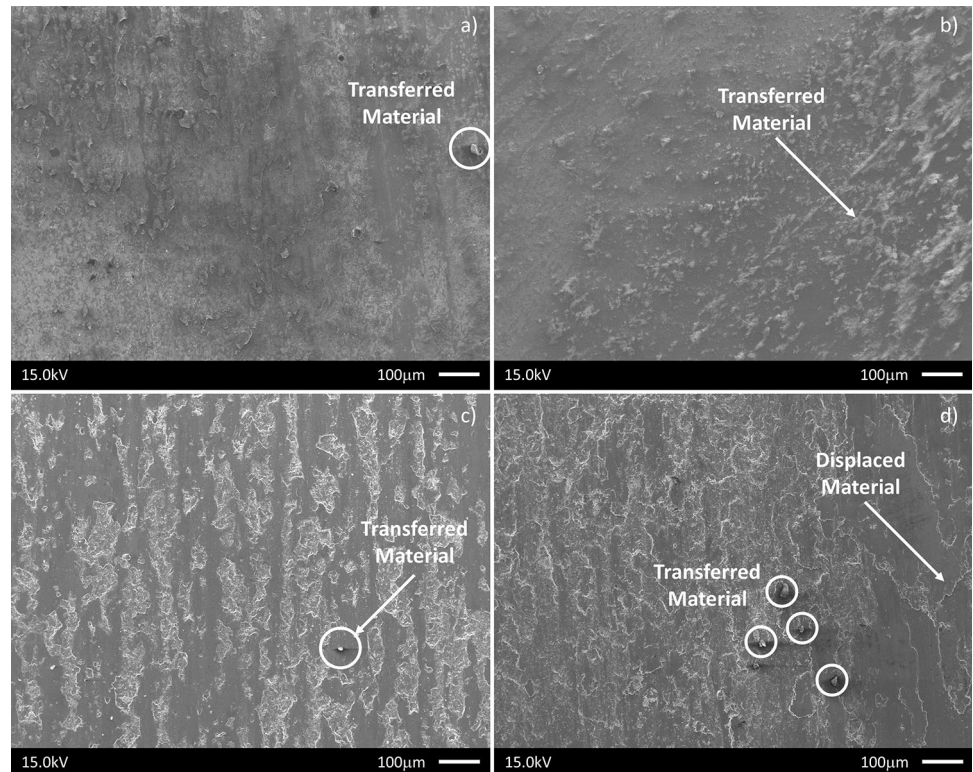


Fig. 9 Volume loss and wear coefficient vs. contact pressure plots for 0.5 m/s

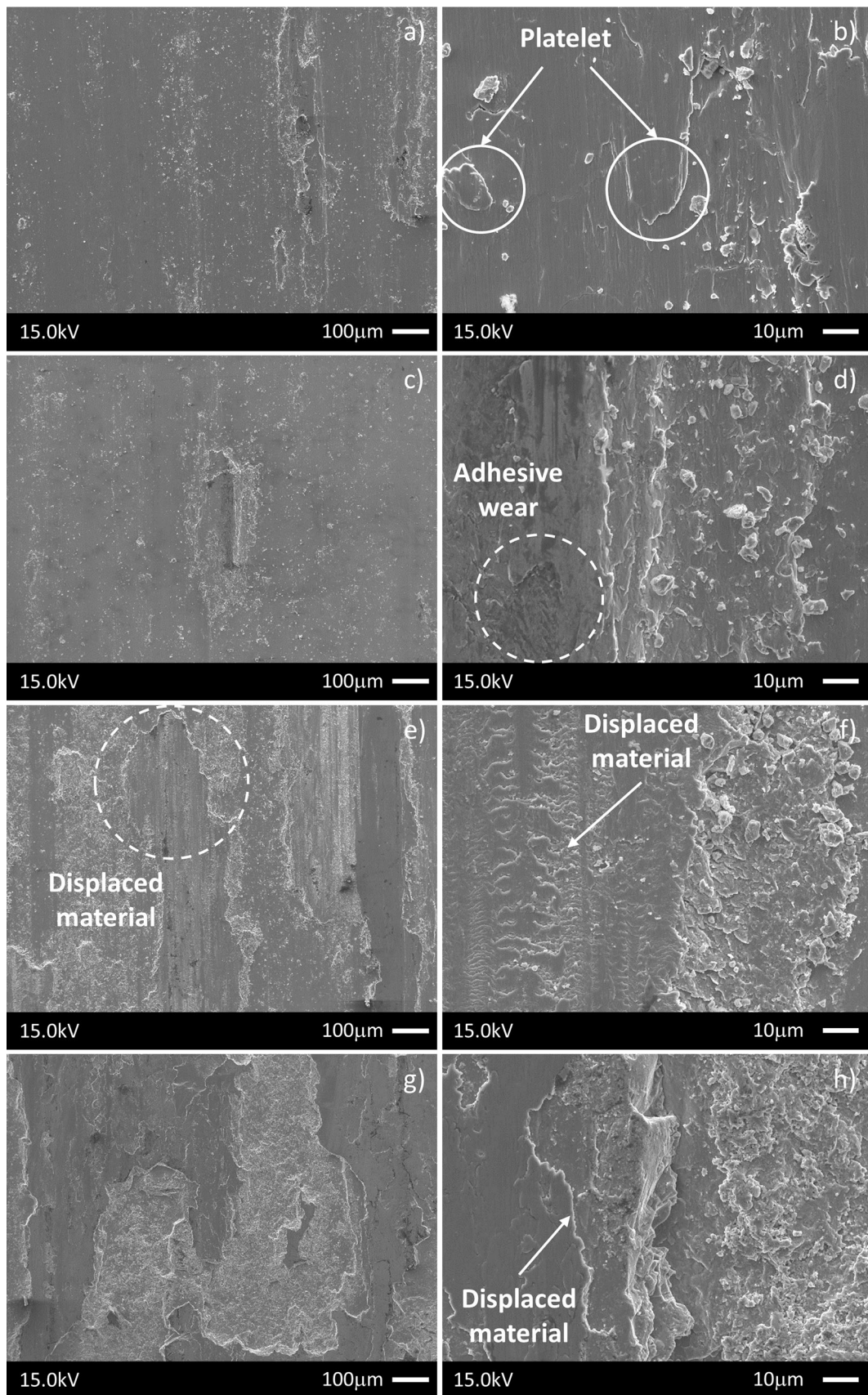


Fig. 10 Representative SEM micrographs of the wear surface of the samples tested at the sliding speed $v = 0.5$ m/s under different contact pressure: (a) and (b) $p = 2$ MPa, (c) and (d) $p = 3$ MPa, (e) and (f) $p = 4$ MPa, (g) and (h) $p = 5$ MPa

speed conditions, further suggesting that material has been highly strained and smeared across the surface covering the underlying sprayed material. A similar phenomenon, considered as “*shear tongues*”, can be seen in laser-clad stellites by Persson (Ref 4). Debris observed throughout all high-speed tests appears to be “plate-like” and consists of smaller broken-up portions of debris that are characterized by a diameter no larger than $10\ \mu\text{m}$ characterized by strained material, displaced across the surface as a consequence of the peeling-off or adhesion of plate-like wear particles. These latter seem to be the consequence of subsurface crack nucleation, observable in the micrograph images of the cross section (see Fig. 5d, e, f), leading to the formation of platelets.

These phenomena, i.e., platelets, subsurface fractures, and displacement of material, were noticeable in the high-speed tests. Due to the physical phenomena observed, the wear mechanisms can be considered a consequence of plastic ratcheting (Ref 41). Plastic ratcheting, in fact, occurs under cyclic loading if the load is high enough to produce a unidirectional accumulation of plastic shear strain with each passing contact. This phenomenon is a consequence of the high stresses experienced under the contact point because residual stresses or work-hardening introduced during the sliding are not enough to avoid further plastic deformation. These plastic strains are primarily responsible for the nucleation of cracks within the coating that propagate parallel to the substrate, as highlighted in Fig. 5. These latter, growing cycle by cycle, lead to the formation of wear particles and once detached are free to be displaced across the wear surface as shown in Fig. 10. In these testing conditions, micrographs of the cross section (see Fig. 5d, e, and f) show subsurface large crack initiation for all tested samples. This is a consequence of the limited material toughness in the direction parallel to the substrate so the weak point of the coating can be found in the cohesion rather than the adhesion to the substrate. The internal porosity, in fact, represents a preferred site for crack initiation. Moreover, due to the higher temperature reached in the contact zone, the adhesion mechanisms occurring between pin and coating can be considered as the main reason for the crack propagation within the coating.

In Fig. 11 are shown the post-wear SEM micrographs of the pins' worn surface and it can be summarized that adhesive wear is the main damage mechanism observable in all high-speed experiments. Deformed material can be identified as trapped wear particles that are visible on as

transferred and adhered material to the worn surface, especially in the tests carried out under 5 MPa of contact pressure (see Fig. 11d). On the contrary, on the worn surface related to the 4 MPa experiments, a type of fatigue wear known as “*nano-grain wear*” can be observed (see Fig. 11c). This phenomenon consists of pulled-out grains which form small globular particles on the wear surface typically clustered around grooves and oxide boundaries.

It can be concluded that with increasing sliding speed, i.e., from 0.1 to 0.5 m/s, a mild-to-severe wear transition occurs. This phenomenon is facilitated by the high temperatures reached in the contact zone as a consequence of the higher value of the sliding speed. This latter is a common phenomenon observable by increasing the loading condition to which the coatings are subjected during wear tests (Ref 42). In fact, with increasing contact pressure, the worn surface appears to be less affected by pull-out phenomena while, due to increased average temperature together with the flash temperature of the pin, the adhesion is more likely to occur, and adhesive wear gradually dominates the wear mechanism. The increasing trend of friction coefficient with the contact pressure, reported in Fig. 4 further suggests an increase in adhesion between pin and sample. It is interesting to note that the evolution of the dynamic friction coefficient as a function of the sliding speed, reported in Fig. 3(b), is almost constant for all values of the contact pressure chosen, suggesting that the wear mechanism involved does not change during the tests.

Nano-indentation Results

The evolution of mechanical properties at the nano-scale was also analyzed with the purpose to capture possible changes in the coating along the thickness and in the region immediately below the worn surface. In this regard, an experimental campaign was carried out by a matrix of 10×10 indentation points with $30\ \mu\text{m}$ spacing between each indent, and with an indentation load of 50 mN.

Low-Speed Tests

The nano-indentation measurements carried out on the cross section of samples tested in low sliding speed conditions ($v = 0.1$ m/s) are reported in Fig. 12. An almost flat trend for both elastic and hardness responses can be observed. However reduced Young's modulus, shown in Fig. 12(a), is lower in the samples tested at a contact pressure of 2 and 3 MPa than in the case of 4 and 5 MPa, with average values of around 218 GPa and 238 GPa, respectively. On the other hand, a different trend was observed in the hardness response, as highlighted in Fig. 12(b), where the measured hardness values seem to be basically unaffected by the contact pressure.

Fig. 11 Representative SEM micrograph of the wear surface on the pin at the sliding speed $v = 0.5$ m/s under different contact pressure: (a) $p = 2$ MPa, (b) $p = 3$ MPa, (c) $p = 4$ MPa, (d) $p = 5$ MPa

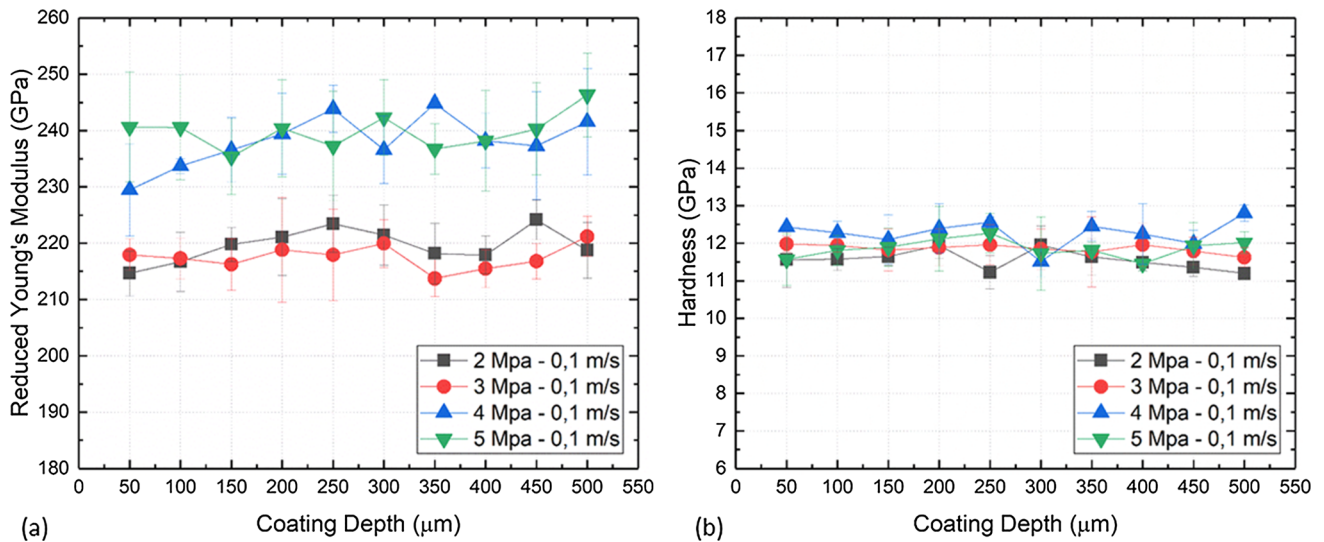
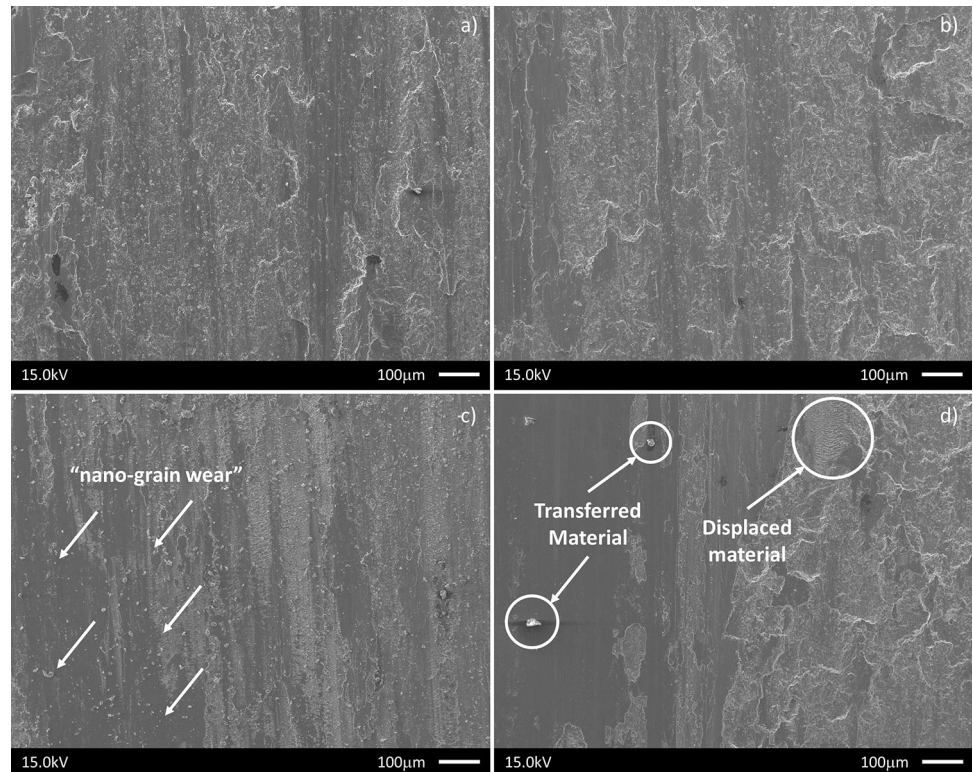


Fig. 12 Plot of the nano-indentation results for reduced elastic modulus and hardness vs. depth for low-speed tests

It is interesting to note that reduced Young’s modulus and hardness, measured on samples tested at 2 and 3 MPa, are extremely close to those measured on the “as-sprayed” coatings, i.e., 212 GPa and 10.2 GPa, respectively, as reported in a previous paper by the authors [37]. The trend observed for stiffness data can be explained by considering that the higher values of the contact pressure tend to close any possible subsuperficial defects below the worn surface. In the previous section, in fact, it was shown that the cross

section of coatings tested at low speed is not characterized by the presence of longitudinal cracks unlike those tested at high speed (see Fig. 5).

These results can be explained considering that hardness response depends only on the plastically deformed volume. On the contrary, the reduced Young’s modulus comes from a bigger volume of material, so the porosity content plays a very important role in the elastic response of the coating. In fact, inter-particle cohesion strength is improved when, as a

consequence of the contact pressure, the defects below the worn surface tend to close and the reduced amount of pores and defects inside the coating prevents possible rigid motions of particles not perfectly adhered to the coatings.

High-Speed Tests

The nano-indentation measurements carried out on the coatings tested at high speed, i.e., $v = 0.5$ m/s, are pointed out in Fig. 13. The obtained results show a reduction in the stiffness (Fig. 13a) and a similar trend in the hardness response (Fig. 13b) as a function of the contact pressure. In addition, it can be noted that this phenomenon is more pronounced in the zones closer to the contact surface. The trends in the hardness can be considered a direct consequence of the high temperature reached during the high-speed tests ($v = 0.5$ m/s). High temperature, in fact, often implies noticeable modifications in the coating microstructure so, this behavior can be related to the grain size evolution of the microstructure. In fact, due to the Hall-Petch effect (Ref 43, 44), the hardness of materials tends to increase with grain refinement as a consequence of enhanced dislocation pile-up at grain boundaries. It can be concluded that the decreasing trend observed in the nano-hardness response could be considered a consequence of grain growth phenomena. Moreover, the observed reduction in the hardness values along the thickness can be also related to the increased presence of cracks inside the coating, clearly observable in Fig. 5(d), (f) and (f).

Regarding the elastic response, the marked reduction in the reduced Young's modulus can be explained by taking into account the presence of cracks and detached material below the surface occurring during the sliding. In fact, a reduction in the elastic modulus is mainly due to the

allowed rigid motions of debonded particles from the coatings during the indentation, and this phenomenon tends to increase by increasing the contact pressure between pin and sample.

Conclusions

A systematic in-depth study on the tribological wear performance of Cold-Sprayed Stellite-6 coatings was carried out in order to better understand the wear mechanisms in reciprocated dry sliding conditions.

Regarding the samples tested in low-speed conditions, they can be summarized:

- Detachment and pull-out phenomena mainly affect the worn surface of coatings.
- Delamination phenomena occur at the intersplat boundaries, and these represent the weak point of the coating.
- A systematic reduction in the dynamic coefficient of friction with the contact pressure has been observed due to the increase in strained oxidized pulled-out particles that act as solid lubricant.

Regarding high-speed tests, instead, it can be summarized as:

- Adhesive wear mechanism can be seen in all tested samples in accordance with the theory of wear for the Steel-CoCr system;
- Plastic deformations occurring during the sliding cause the crack initiation and propagation within the coating, usually at splat boundaries or in correspondence of pores;

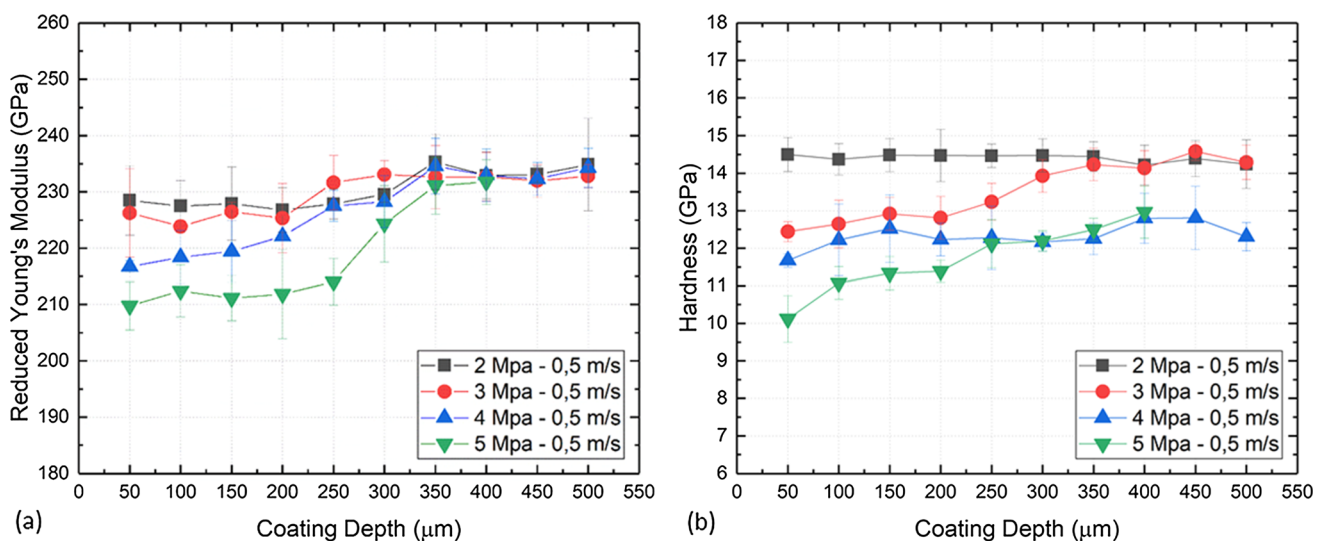


Fig. 13 Plot of the nano-indentation results for reduced elastic modulus and hardness vs. depth for high-speed tests

- Material is displaced toward the coating surface then, due to elastic fracture, detachment of the material results in wear-particles;
- Debris is thin and plate-like consisting of smaller broken-up portions of detached particles characterized by strained material, displaced across the surface.

The cross-sectional nano-indentation tests revealed a different response in the samples tested in low-speed and high-speed conditions:

- An increase in stiffness with the applied load was observed when sliding speed was set equal to 0.1 m/s, due to the closure of subsurface defects below the worn surface, with a consequent reduction in the porosity and an increase in the cohesion strength. However further study is needed to clarify this hypothesis.
- A reduction in the stiffness and hardness response as a function of the contact pressure was observed in the case of sliding speed equal to 0.5 m/s, due to the increased presence of cracks inside the coating.

Acknowledgment Nanoindentation experiments were carried out in the “MaTeRiA Laboratory” (University of Calabria), funded by “Pon Ricerca e Competitività 2007/2013.” Wear experiments were carried out at the national Centre for Advanced Tribology at Southampton (nCATS). The authors would like to give special thanks to Dr. Zaihao Tian for performing the SEM analysis.

Funding Open access funding provided by Università della Calabria within the CRUI-CARE Agreement.

Open Access This article is licensed under a Creative Commons Attribution 4.0 International License, which permits use, sharing, adaptation, distribution and reproduction in any medium or format, as long as you give appropriate credit to the original author(s) and the source, provide a link to the Creative Commons licence, and indicate if changes were made. The images or other third party material in this article are included in the article’s Creative Commons licence, unless indicated otherwise in a credit line to the material. If material is not included in the article’s Creative Commons licence and your intended use is not permitted by statutory regulation or exceeds the permitted use, you will need to obtain permission directly from the copyright holder. To view a copy of this licence, visit <http://creativecommons.org/licenses/by/4.0/>.

References

1. P. Crook, Cobalt and Cobalt Alloys, *Properties and Selection: Nonferrous Alloys and Special-Purpose Materials*, ASM International, 1990.
2. U. Malayoglu, A. Neville, and H. Lovelock, Assessing the Kinetics and Mechanisms of Corrosion of Cast and HIPed Stellite 6 in Aqueous Saline Environments, *Corros. Sci.*, 2005, **47**(8), p 1911-1931.
3. Š Houdková, Z. Pala, E. Smazalová, M. Vostřák, and Z. Česánek, Microstructure and Sliding Wear Properties of HVOF Sprayed, Laser Remelted and Laser Clad Stellite 6 Coatings, *Surf. Coat. Technol.*, 2017, **318**, p 129-141.
4. D.H.E. Persson, *On the Mechanisms behind the Tribological Performance of Stellites (PhD Dissertation)*, Acta Universitatis Upsaliensis, Uppsala, 2005.
5. J.W. Christian, Equilibrium and General Kinetic Theory, *The Theory of Transformations in Metals and Alloys*, J.W. CHRISTIAN, Ed., (Oxford), Pergamon, 2002, p 1-22.
6. J.C. Shin, J.M. Doh, J.K. Yoon, D.Y. Lee, and J.S. Kim, Effect of Molybdenum on the Microstructure and Wear Resistance of Cobalt-Base Stellite Hardfacing Alloys, *Surf. Coat. Technol.*, 2003, **166**(2-3), p 117-126.
7. R. Arabi Jeshvaghani, M. Shamanian and M. Jaberzadeh, Enhancement of Wear Resistance of Ductile Iron Surface Alloyed by Stellite 6, *Mater. Des.*, 2011, **32**(4), p 2028-2033.
8. A.S.C.M. D’Oliveira, R. Vilar, and C.G. Feder, High Temperature Behaviour of Plasma Transferred Arc and Laser Co-Based Alloy Coatings, *Appl. Surf. Sci.*, 2002, **201**(1-4), p 154-160.
9. A. Kusmoko, A.D. Dunne and, H.A. Li, A Comparative Study for Wear Resistant of Stellite 6 Coatings on Nickel Alloy Substrate Produced by Laser Cladding HVOF and Plasma Spraying Techniques, *Int. J. Curr. Eng. Technol.*, 2014, **4**(1), p 32-36.
10. T.S. Sidhu, S. Prakash, and R.D. Agrawal, Hot Corrosion Studies of HVOF NiCrBSi and Stellite-6 Coatings on a Ni-Based Superalloy in an Actual Industrial Environment of a Coal Fired Boiler, *Surf. Coat. Technol.*, 2006, **201**(3-4), p 1602-1612.
11. T.S. Sidhu, S. Prakash, and R.D. Agrawal, Hot Corrosion Resistance of High-Velocity Oxyfuel Sprayed Coatings on a Nickel-Base Superalloy in Molten Salt Environment, *J. Therm. Spray Technol.*, 2006, **15**(3), p 387-399.
12. H.S. Sidhu, B.S. Sidhu, and S. Prakash, Solid Particle Erosion of HVOF Sprayed NiCr and Stellite-6 Coatings, *Surf. Coat. Technol.*, 2007, **202**(2), p 232-238.
13. N. Jegadeeswaran, K.U. Bhat, and M.R. Ramesh, Oxidation Studies on As-Received and HVOF Sprayed Stellite-6 Coating on Turbine Alloys at 800°C, *Int. J. Sci. Eng. Res.*, 2013, **4**(6), p 214-220.
14. L. Moskowitz and K. Trelewicz, HVOF Coatings for Heavy-Wear, High-Impact Applications, *J. Therm. Spray Technol.*, 1997, **6**(3), p 294-299.
15. A. Kumar, J. Boy, R. Zatorski, and L.D. Stephenson, Thermal Spray and Weld Repair Alloys for the Repair of Cavitation Damage in Turbines and Pumps: A Technical Note, *J. Therm. Spray Technol.*, 2005, **14**(2), p 177-182.
16. A. Frenk, M. Vandyoussefi, J.D. Wagniere, A. Zryd, and W. Kurz, Analysis of the Laser-Cladding Process for Stellite on Steel, *Metall. Mater. Trans. B*, 1997, **28**(3), p 501-508.
17. V. Ocelík, U. de Oliveira, M. de Boer, and J.T.M. de Hosson, Thick Co-Based Coating on Cast Iron by Side Laser Cladding: Analysis of Processing Conditions and Coating Properties, *Surf. Coat. Technol.*, 2007, **201**(12), p 5875-5883.
18. V. Ocelík, M. Eekma, I. Hemmati, and J.T.M. De Hosson, Elimination of Start/Stop Defects in Laser Cladding, *Surf. Coat. Technol.*, 2012, **206**(8-9), p 2403-2409.
19. A. Kusmoko, D. Dunne, H. Li, and D. Nolan, Effect of Two Different Energy Inputs for Laser Cladding of Stellite 6 on P91 and P22 Steel Substrates, *Procedia Mater. Sci.*, 2014, **6**, p 26-36.
20. A.S.C.M. D’Oliveira, P.S.C.P. Da Silva, and R.M.C. Vilar, Microstructural Features of Consecutive Layers of Stellite 6

- Deposited by Laser Cladding, *Surf. Coat. Technol.*, 2002, **153**(2-3), p 203-209.
21. U. de Oliveira, V. Ocelík, and J.T.M. De Hosson, Microstresses and Microstructure in Thick Cobalt-Based Laser Deposited Coatings, *Surf. Coat. Technol.*, 2007, **201**(14), p 6363-6371.
 22. A. Gholipour, M. Shamanian, and F. Ashrafzadeh, Microstructure and Wear Behavior of Stellite 6 Cladding on 17-4 PH Stainless Steel, *J. Alloys Compd.*, 2011, **509**(14), p 4905-4909.
 23. R. Singh, D. Kumar, S.K. Mishra, and S.K. Tiwari, Laser Cladding of Stellite 6 on Stainless Steel to Enhance Solid Particle Erosion and Cavitation Resistance, *Surf. Coat. Technol.*, 2014, **251**, p 87-97.
 24. H. Assadi, H. Kreye, F. Gärtner, and T. Klassen, Cold Spraying—A Materials Perspective, *Acta Mater.*, 2016, **116**, p 382-407.
 25. T. Schmidt, H. Assadi, F. Gärtner, H. Richter, T. Stoltenhoff, H. Kreye, and T. Klassen, From Particle Acceleration to Impact and Bonding in Cold Spraying, *J. Therm. Spray Technol.*, 2009, **18**(5-6), p 794-808.
 26. T. Stoltenhoff, H. Kreye, and H.J. Richter, An Analysis of the Cold Spray Process and Its Coatings, *J. Therm. Spray Technol.*, 2002, **11**(4), p 542-550.
 27. H. Assadi, F. Gärtner, T. Stoltenhoff, and H. Kreye, Bonding Mechanism in Cold Gas Spraying, *Acta Mater.*, 2003, **51**(15), p 4379-4394.
 28. A. Moridi, S.M. Hassani-Gangaraj, M. Guagliano, and M. Dao, Cold Spray Coating: Review of Material Systems and Future Perspectives, *Surf. Eng.*, 2014, **30**(6), p 369-395.
 29. A. Sova, I. Smurov, M. Doubenskaia, and P. Petrovskiy, Deposition of Aluminum Powder by Cold Spray Micronozzle, *Int. J. Adv. Manuf. Technol.*, 2018, **95**(9-12), p 3745-3752.
 30. S.L. Fu, C.X. Li, Y.K. Wei, X.T. Luo, G.J. Yang, C.J. Li, and J.L. Li, Novel Method of Aluminum to Copper Bonding by Cold Spray, *J. Therm. Spray Technol.*, 2018, **27**(4), p 624-640.
 31. P. Sirvent, M.A. Garrido, C.J. Múñez, P. Poza, and S. Vezzù, Effect of Higher Deposition Temperatures on the Microstructure and Mechanical Properties of Al 2024 Cold Sprayed Coatings, *Surf. Coat. Technol.*, 2018, **337**, p 461-470.
 32. H. Yu, R. Ahmed and H. de V. Lovelock, and S. Davies, Influence of Manufacturing Process and Alloying Element Content on the Tribomechanical Properties of Cobalt-Based Alloys, *J. Tribol.*, 2009, **131**(1), p 1-12.
 33. A. Frenk and W. Kurz, Microstructural Effects on the Sliding Wear Resistance of a Cobalt-Based Alloy, *Wear*, 1994, **174**(1-2), p 81-91.
 34. T. Roy, Q. Lai, R. Abrahams, P. Mutton, A. Paradowska, M. Soodi, and W. Yan, Effect of Deposition Material and Heat Treatment on Wear and Rolling Contact Fatigue of Laser Cladded Rails, *Wear*, 2018, **412-413**, p 69-81.
 35. J.F. Archard, Contact and Rubbing of Flat Surfaces, *J. Appl. Phys.*, 1953, **24**(8), p 981-988.
 36. V. Hegadekatte, N. Huber, and O. Kraft, Finite Element Based Simulation of Dry Sliding Wear, *Model. Simul. Mat. Sci. Eng.*, 2005, **13**(1), p 57-75.
 37. P. Magarò, A.L. Marino, A. Di Schino, F. Furgiuele, C. Maletta, R. Pileggi, E. Sgambitterra, C. Testani, and M. Tului, Effect of Process Parameters on the Properties of Stellite-6 Coatings Deposited by Cold Gas Dynamic Spray, *Surf. Coat. Technol.*, 2019, **377**, p 124934.
 38. P. Magarò, A.L. Marino, C. Maletta, M. Tului, and A. Di Schino, Tribological Properties of Wear-Resistant Coatings Obtained by Cold Gas Dynamic Spray, *Procedia Struct. Integ.*, 2018, **9**, p 287-294.
 39. P.S.G. Cross, G. Limbert, D. Stewart, and R.J.K. Wood, Ratcheting Wear of a Cobalt-Chromium Alloy during Reciprocated Self-Mated Dry Sliding, *Wear*, 2019, **426-427**, p 1142-1151.
 40. R. Büscher, G. Täger, W. Dudzinski, B. Gleising, M.A. Wimmer, and A. Fischer, Subsurface Microstructure of Metal-on-Metal Hip Joints and Its Relationship to Wear Particle Generation, *J. Biomed. Mater. Res. B Appl. Biomater.*, 2005, **72**(1), p 206-214.
 41. A. Kapoor, Wear by Plastic Ratcheting, *Wear*, 1997, **212**(1), p 119-130.
 42. W. Gao, Y. Lian, G. Xie, J. Huang, L. Zhang, M. Ma, C. Zhao, Z. Zhang, K. Liu, S. Zhang, and J. Zhang, Study of Dry Sliding Wear Characteristics of Stellite 6B versus AISI M2 Steel at Various Sliding Velocities, *Wear*, 2018, **402-403**, p 169-178.
 43. H.S. Kim and M.B. Bush, Effects of Grain Size and Porosity on the Elastic Modulus of Nanocrystalline Materials, *Nanostruct. Mater.*, 1999, **11**(3), p 361-367.
 44. A. Latapie and D. Farkas, Effect of Grain Size on the Elastic Properties of Nanocrystalline α -Iron, *Scr. Mater.*, 2003, **48**(5), p 611-615.

Publisher's Note Springer Nature remains neutral with regard to jurisdictional claims in published maps and institutional affiliations.